scientific reports

Check for updates

OPEN

Enhancement in electrical conductivity of liquid crystals by graphene metal oxide composites

M. Khodaee[1], N. Dalir[2], F. Feghhi[3], N. Ansari[3], M. Mohammadimasoudi[4], A. Goudarzi[4], A. F. Nasiri[1], M. Kolahdouz[1]✉ & SM. Mohseni[5]✉

Enhancing the electrical conductivity of liquid crystal (LC) circumvents challenges for application in advanced electronic components. Toward this, using additives made of different nanostructures that could result in functional LCs is suggested. In this paper, various concentrations of graphene (Gr)/metal-oxide (Fe_3O_4) nanocomposite (GMN) (0.0001–1 w%) were added to E7 nematic LC. We found that the role of anisotropic Gr flakes, their edges as well as surface-decorated-metal-oxide-additives have significant impact on electrical properties of E7. A range of appropriate additives of such a nanocomposite enhances the electrical conductivity of LCs. This effect can be traced through the decrease in the formation of GMN aggregates in the E7 and increase in the electrostatic field at the edges of the Gr sheets. Moreover, the presence of metal-oxide nanoclusters due to the presence of oxygen vacancies and defects facilitates the construction of conductive network for improving the charge transfer pathways and contributes to a stronger interaction of the Gr surface with charged species. These factors can provide Gr layers as dipole moments and lead to signal propagation in the dielectric medium. Our finding conveys a pathway toward significant enhancement of electrical conductivity in the LC family which can be useful for functional applications.

Doping liquid crystals (LCs) with nanomaterials addresses an important strategy for tuning their properties[1]. Doped LCs exhibit significantly improved properties compared to their undoped ones, while they also achieve long-term stability for industrial applications[2–5]. It has been shown that low loadings of various nanomaterials with zero-, one-, and two-dimensional structures dispersed in LCs media can significantly affect their physical properties, especially space-charge distribution[6–11]. For instance, electro-optical response as well as the electrical behavior of LCs can be influenced by such doping[12,13]. In this regard, two major factors of nanomaterials, i.e. their surface-to-volume ratio, as well as their interactions between active agents and ions of LCs can make them promising candidates for demanding applications[14].

Improvement of electrical conductivity of LCs due to doping can also influence their properties for more functional applications[15]. To date, this has been achieved through the inclusion of high concentrations of nanomaterials in LCs which can lead to the amplification of ionic conductivity[11] and degradation of the electro-optical response due to aggregate formation[16]. Moreover, in the cases of chain and network formation, the enhancement in DC conductivity can disturb the LC properties. Studies have shown this effect for LCs doped by nanoparticles made from carbon nanotubes, metals, and polymeric inclusions[6,17–19]. Alternatively, better exploitation of liquid crystalline behavior for demanding applications needs an understanding of ionic phenomena in LCs doped with nanomaterials[20,21] and identification of processes that lead to the purification of LCs with optimal values of nanomaterials[14,15,22,23]. Considering the attempts leading to optimization of LC properties in some fields by functionalizing nanoparticles[11,24,25], purification along with conductivity improvement requires using low concentrations of nanomaterials in LCs. Hence, nanomaterials need to be surface-treated differently[26] for tuning their effective role within LCs.

[1]School of Electrical and Computer Engineering, College of Engineering, University of Tehran, Tehran 1439957131, Iran. [2]Department of Renewable Energy, Interdisciplinary Science and Technology, Tarbiat Modares University, Tehran 14115-175, Iran. [3]Department of Physics, Alzahra University, Tehran 19938, Iran. [4]Nano-Bio-Photonics Lab, Faculty of New Sciences and Technologies, University of Tehran, Tehran 1439957131, Iran. [5]Department of Physics, Shahid Beheshti University, Evin, Tehran 19839, Iran. ✉email: kolahdouz@ut.ac.ir; m-mohseni@sbu.ac.ir

Graphene (Gr) is one of the well-known 2D nanomaterials that can manipulate the electrical properties of LCs[27–37]. The effectiveness of Gr layers in different phases of LCs often leads to two outcomes: (I) When Gr sheets mix with LC, their electrostatic field and screening effect leads to the suppression of ionic behaviors such as reduction in ionic density, diffusivity, conductivity, and relaxation frequency through the ion trapping/charge annihilation process[22]; (II) The interaction between the honeycomb pattern of Gr and the benzene rings of LC molecules causes the LC directors to planar stabilize on the surface of the Gr layers and results in the improvement of dielectric anisotropy[38].

However, in both cases, the function of Gr is limited to serving as alignment layers for molecules of host LCs. Moreover, considering that strong van der Waals interactions between Gr layers tend to cause Gr re-stacking together with the oxidation effects during the synthesis process, these problems lead to the loss or even deprivation of the diffusion rate and excellent specific surface area of Gr, limiting its applications in various fields[39–41].

One of the most efficient solutions to overcome these problems is to functionalize Gr sheets with oxygen-containing groups such as transition metal-oxides with excellent oxygen evolution reactions (OER)[42]. This not only enhances the adsorption process but also facilitates the construction of a 3D porous conductive network for improving the charge transfer pathways and electrical properties[43,44]. In addition, the Gr surface provides nucleation sites for the in-situ growth of the metallic nanoparticles between their successive layer formation that prevents their agglomeration[45,46]. Such metal-oxide formation decorated at the surface of Gr layers includes vacancies and defects that play as active sites adjacent to LCs for improving conductivity and inducing functionality.

It has also demonstrated nanomaterials of Gr and metal-oxide agents are considered to be potential candidates for charge trapping and their electric field-controlled effects[47]. Family of various metals such as Fe, Cu, and Ag can be suggested to provide active sites adjacent to Gr plates. They are thus suitable for deployment as doping agents in LCs to control LC response against the electric field. Interestingly, migration of oxygen vacancies and metal cations via the electric field in such materials influences chemical activity and conductivity of the product[48,49].

To achieve LCs with controlled conductivity through doping agents, in this paper, we used air-stable multi-layer Gr (MLG) hosting metal-oxide Fe_3O_4-nanoclusters as an additive to E7 nematic LC. This Gr/metal-oxide-nanocomposite (GMN) is achieved through the electrochemical exfoliation of graphite[50–52], which produces a scalable Gr product and the simultaneous deposition of Fe_3O_4 nanoclusters on the surface of Gr layers in a suitable solution[53]. Different concentrations of this hybrid within the E7 are investigated to realize the dual purpose of prevention of aggregation formation in LC and improvement of its conductivity, using polarizing optical microscopy (POM) and also the powerful impedance spectroscopy tool.

Results and discussion

Figure 1 shows the results of the GMN characterization. The FESEM and TEM analysis (Fig. 1a–c) validate the formation of micron boundary size of Gr multi-layered structure and Fe_3O_4 nanoclusters distributed randomly on its layers. In Fig. 1b, the closer we get to the edges of Gr layer, the more aggregations of nanoclusters are formed. Although, the dimensions of some of them are below 35 nm. Figure 1d shows another TEM view of nanoclusters near the edge of the Gr layer. According to this analysis, there are hexagonal structures, some of which are stacked or rolled up, which are related mainly to Fe_3O_4 nanocrystals. Furthermore, the examination of the XRD pattern of this nanocomposite confirms the presence of Fe_3O_4 peaks at defined 2θ positions. Also, the presence of these peaks on a non-smooth line may indicate the formation of some of the Fe_3O_4 structures in the amorphous phases. This data also shows the typical crystalline structure of graphite in the material. In fact, the XRD pattern of graphite has a sharp and tight peak at 26° which corresponds to the diffraction line C (002)[54]. However, through the exfoliation process, this high-intensity characteristic has degraded to some extent, and instead a broad mound corresponding to the graphene is added.

The POM images of texture changes for dispersions of GMN in E7 at different concentrations (0.0001–1 w%) have shown in Fig. 2. The 0.0001 w% sample (Fig. 2a) has a relatively uniform texture, indicating a homogeneous distribution of the nanocomposite within the LC. In fact, in this case, the concentration of nanocomposite is low enough to minimize aggregation formation within the LC. In the 0.001 w% sample (Fig. 2b), aggregates with maximum dimensions of 20 µm appear apart from each other. In the 0.01 w% sample, these aggregates connected in places, and finally, in Fig. 2d, the sample was dominated by separately large aggregations of the GMN. Although there is no trace of the chain formation of aggregates up to the concentration of 1 w% GMN dopant in the E7, these aggregates affect the electrical properties of the samples, especially for dopant concentrations of (0.01–1 w%), which will be discussed later.

Impedance spectroscopy is an efficient method for tracking the behavior of mobile ions in the bulk and interfacial regions of fluids. Experimental data for the magnitude $|Z| = \sqrt{Z_r^2 + Z_i^2}$ and phase angle $\Phi = \arctan(Z_i/Z_r)$ of complex impedance, in which Z_r denotes the active component, and Z_i denotes the reactive component, are depicted in Fig. 3. The process of changing the impedance value for pure E7, as depicted with blue symbols in Fig. 3a, can be divided into four parts in the overall frequency range. As the frequency increases from 100 mHz to 2 Hz (part I), the magnitude of impedance has a decreasing trend and then this slope flattens out and gets a plateau of a relatively-constant value over a broad frequency range (2–158.5 Hz) (part II). For frequencies above 158.5 Hz up to nearly 6.3 kHz (part III), the second linearly decreasing trend occurs. Finally, for frequencies more than 6.3 kHz (part IV), the magnitude of the impedance reaches a constant value. The phase angle for frequencies more than 6.3 kHz remains within the extent of − 85° to − 89° and as the frequency decreases, the phase response reaches a maximum with the value of − 3.89°, which corresponds to the saddle point at the frequency of about 15.85 Hz, and then it decreases until the reach to the frequency of 100 mHz. In other words, from 100 mHz to 15.85 Hz, molecules present at the interface interact with the electric field, but in the range 15.85 Hz to 1 MHz, the LC dipole moment begins to interact with the electric field[13,55].

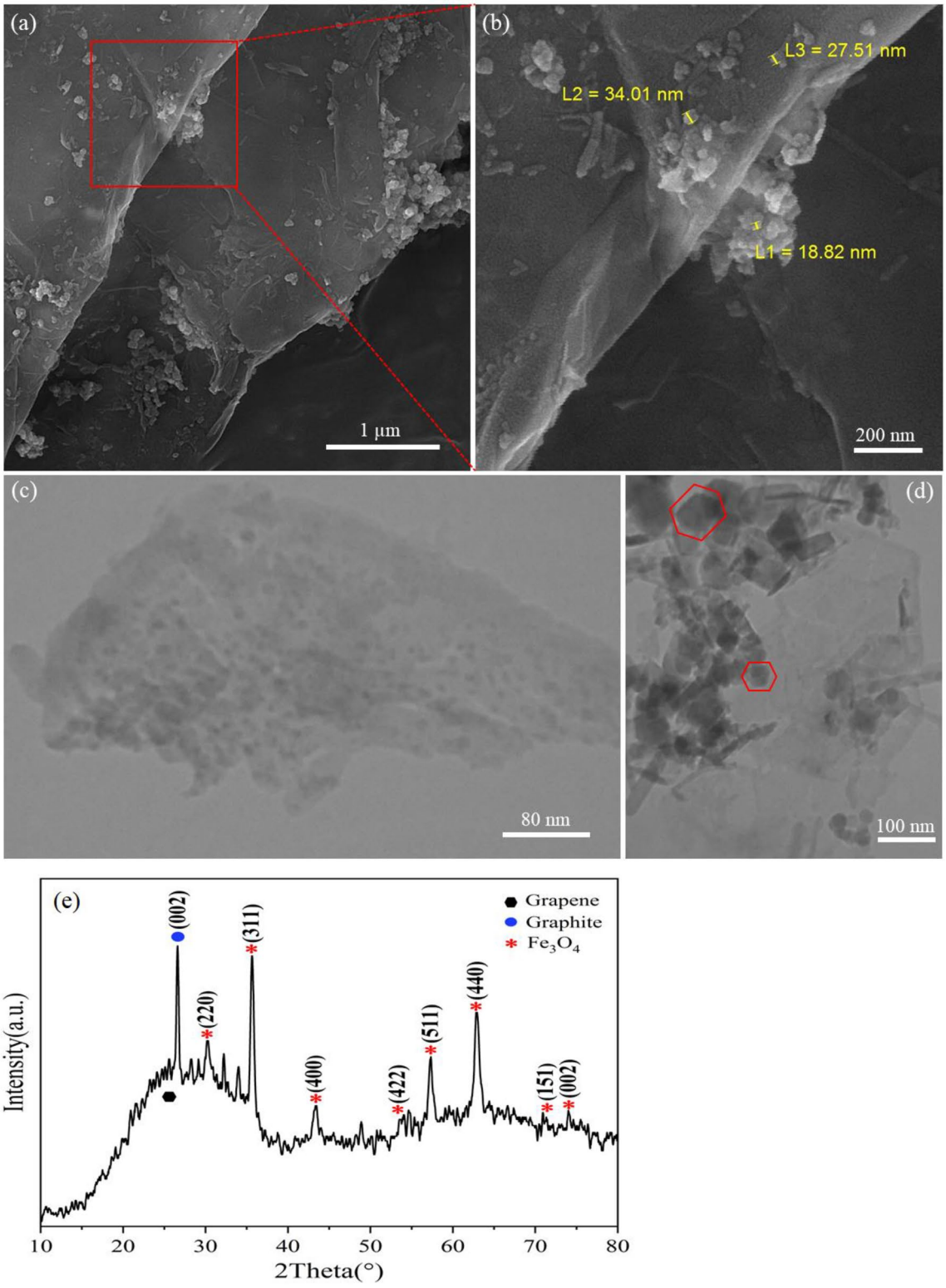

Figure 1. (**a**,**b**) FESEM images of GMN and different size of Fe_3O_4 nanoclusters especially in the edges of the Gr layers and (**c**,**d**) TEM images of a micron boundary size of Gr sheet and different geometry of Fe_3O_4 samples indicating well distribution of Fe_3O_4 nanoclusters on the Gr layers. (**e**) XRD pattern of GMN, showing well exfoliation of graphite and formation of the Gr layers.

As shown in Fig. 3, the addition of GMN with different concentrations (0.0001–1 w%) to the E7 leads to a shift in the impedance data to higher frequencies. Of course, the lower the dopant concentration, the more the

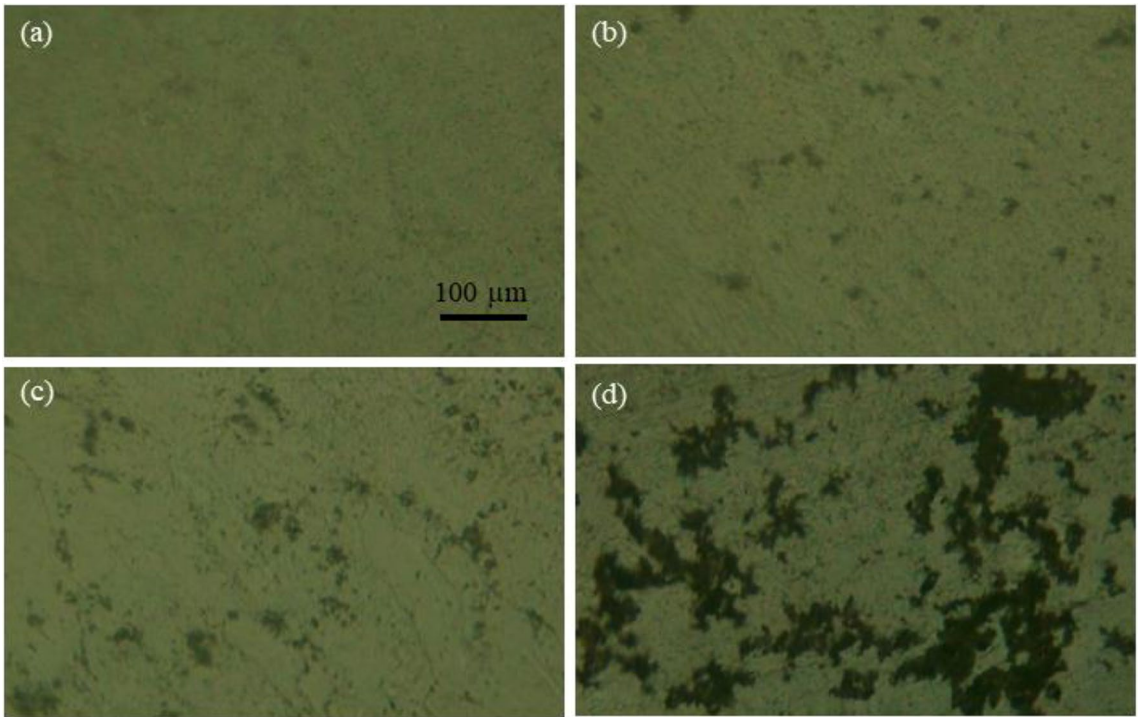

Figure 2. The images of texture changes in (**a**) 0.0001 w%, (**b**) 0.001 w%, (**c**) 0.01 w%, (**d**) 1 w% GMN-doped samples observed under POM. The cells are placed between parallel polarizer and analyzer.

frequency shift. More details are as follows: The impedance value and phase response, for all of the doped samples in part IV, tend to be constant nearly to the pure E7 response, which results in the conclusion that in this part, the reactive component of the impedance is dominant and we are facing primarily capacitive behavior. In the first three parts with decreasing frequency, the impedance values of the doped samples follow the general trend of pure E7. However, their impedance values are lower compared to E7, and the smaller the amount of GMN dopant, the more the drop in impedance values. This general principle continues in the first part down to a frequency of 0.25 Hz, and then for the lower frequencies is broken by the 1 w% and 0.01 w% samples whose impedance values exceed that assumed by pure E7. In Table 1S (SI), these changes were analyzed quantitatively. As seen in Fig. 3a, the behavior of doped samples is divided into two categories due to the similarity of the responses in impedance magnitude. Those samples inside the range of (0.01–1 w%) are in the first category and those within the range of (0.0001–0.001 w%) are in the second one. The main difference in appearance between these two categories is the size of aggregations which will be discussed later. One can derive the behavior of a capacitor with a residual leakage current from the impedance response of the diagrams in Fig. 3.

To get a better idea of the electrical behavior of the samples, the Cole–Cole plots are also included in Fig. 4a. The Cole–Cole plot of pure E7 appears in a semicircle and a Warburg impedance, and this form of reaction has been confirmed by all of the GMN-doped samples. This semicircle represents the mid-range frequency response of the system, and its diameter indicates the bulk resistance of the LC, which is reduced by the addition of the GMN dopant. Noteworthy is the direct relationship between the dopant concentration and the magnitude of its bulk resistance. The lower the dopant concentration, the more the bulk resistance decreases.

A quantitative review of the above-mentioned topics is provided by presenting the electrical equivalent circuit (EEC) model in Fig. 4b. Here, the EEC model can be defined as the series connection of the following three parts: the part related to the resistance of the electrodes and connectors R_{CR}, the part related to the high frequencies (100 Hz–100 kHz) caused by the reaction of LC molecules to the electric field and characterized by the parallel connection of R_{LC}, the active component and C_{LC}, the reactive component of the bulk of LC[17,56,57], and the part associated with low frequencies (100 mHz–100 Hz) which considered the reaction of spaced charges in the vicinity of the electrodes and consists of the parallel connection of C_{DL}, the double layer capacitance and W, finite diffusion Warburg element[57–59]. The Warburg element itself consists of two parts: W_{sr}, Warburg coefficient in bulk and W_{sc}, Warburg coefficient in double layer[11]. More details are available in the SI.

The solid lines in Fig. 4a depict the good-fitting results of retrieving the cole–cole plot for each sample using this EEC model, and Table 1 displays the values obtained for each component. The obtained results are as follows: The resistance of connectors and electrodes R_{CR} is not affected by doping of GMN ($R_{CR} = 0.2 \pm 0.04\ k\Omega$). Furthermore, the reactive component of the bulk, C_{LC}, which is related to the permittivity of the LC, remains constant upon dopant addition ($C_{LC} = 110.1 \pm 14.1$ pF). Albeit a small deviation is expected from slightly different cell gaps. The data obtained from C_{LC} were also used to calculate the real, ε_r, and imaginary, ε_i, part of the complex dielectric permittivity, $\varepsilon = \varepsilon_r - i\varepsilon_i$, and its magnitude, $\Delta\varepsilon$, for pure and doped E7 samples, which generally indicates that the values obtained for each dielectric parameter of doped samples are higher than the values obtained for pure one.

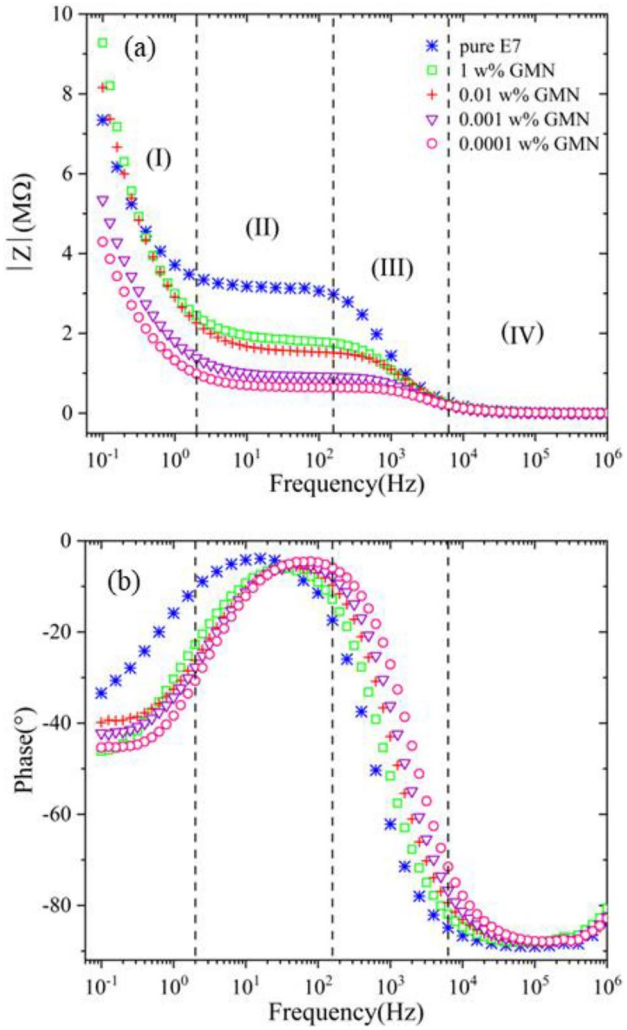

Figure 3. (**a**) Impedance magnitude and (**b**) phase angle vs. frequency for pure and GMN-doped E7.

Considering that these parameters were obtained at frequencies at which ionic contaminants and spaced charges cannot follow the polarization of the applied electric field, these results are reasonable.

In addition, in the low-frequency part, due to the dispersion in the values of the double-layer capacitor, a clear relationship between it and the dopant concentration cannot be obtained. Of course, C_{DL} is three orders of magnitude larger than the bulk capacitance and dominates the impedance spectra at sufficiently low frequencies.

A strong effect of GMN doping is found for the bulk resistance, R_{LC}, which is caused by residual impurities in the LC. It decreases from 3.12 MΩ/cm^2 for pure E7 to 0.646 MΩ/cm^2 for 0.0001 w% sample. This decrease in bulk resistance of the samples can be equated with the increase in the relevant electrical conductivity[60]. The inverse trend of increasing this electrical conductivity with decreasing dopant concentration indicates that ionic impurities have no significant contribution to this increasing trend. Furthermore, considering the planar alignment of the Gr sheets in accordance with the E7 nematic director, to reduce the elastic distortion of the nematic matrix, these sheets act as insulators for the propagation of the applied electric field[22]. Therefore, improving conductivity using a low concentration of GMN dopant should be sought after.

(i) LCs are insulators and their conductivity is due to the presence of ionic impurities nominated as ionic conductivity[7]. Gr sheets are potential source of ionic impurities and near their edges electrostatic field is strong. This is more significant when Gr sheets are corrugated or they have small lateral sizes[61]. Hence, they can trap ionic impurities in dielectric media and reduce the ionic conductivity. Meanwhile, the effects related to metal-oxide nanoclusters between Gr layers cannot be ignored. The presence of Fe_3O_4 nanoclusters, in addition to enriching the surface of Gr layers with metal ions, also increases its interaction in the LC medium. At sufficiently low frequencies, different redistributions of oxygen vacancies and defects in these nanoclusters in response to the applied electric field lead to the formation of nano-conductive areas on the surface of Gr layers which facilitate the charge transfer[47,62,63]. These effects are particularly pronounced at the edges of Gr layers, which tend to accumulate more charged species. These factors can make Gr layers act as dipole moments, resulting in the creation

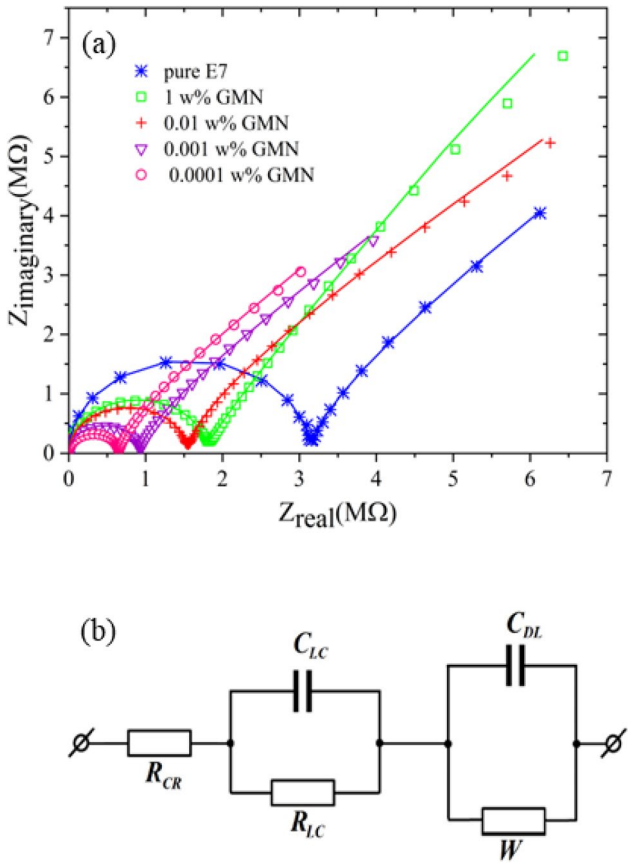

Figure 4. (**a**) The Cole–Cole plots and (**b**) equivalent electrical circuit model for pure and GMN-doped E7. The fitted lines are shown by solid lines in part (**a**).

Sample	R_{CR} (kΩ)	R_{LC} (MΩ/cm^2)	C_{LC} (pF)	C_{DL} (nF)	W_{sr} (MΩ·s$^{-1/2}$)	W_{sc} (Ω·s$^{-1/2}$)	ε_r	ε_i	Δε
Pure E7	0.163	3.12	96.85	75.8	31.23	45.36	4.2	3.49	5.46
1% GMN	0.241	1.78	112	20.5	39.28	18.88	4.99	4.97	7.04
0.01% GMN	0.188	1.53	96	35.28	39.58	49.69	4.15	4.47	6.10
0.001% GMN	0.169	0.92	124.2	55.33	26.12	40.77	5.60	6.17	8.33
0.0001% GMN	0.160	0.646	121.5	82.37	29.60	69	5.38	5.45	7.65

Table 1. Nominal parameters for the elements of the EEC model as obtained by fitting the EEC response to the experimental data.

of dipolar fields and signal propagation in the direction perpendicular to the cell. Moreover, the smaller the aggregations, the more effective areas are available for the Gr layers to absorb the space charges thus leading to the enhancement of conductivity. This is important to note that GMN dopant can act as a source of ions and upon dispersing them within the LC, some fraction of these ions can be released into the bulk. However, the used E7 LC initially contains a considerable amount of ionic impurities, and its electrical conductivity is in the range of 10^{-7} S/m. Moreover, investigation of the process of changes in bulk resistance (or related electrical conductivity) value in all samples especially those with the lowest amount of dopant concentration, suggests the dominant behavior of ion trapping by dopants[21].(ii) Gr is able to anchor active components to its surface. Gr's large area acts as an alignment layer that exerts another anchoring successively and induces a short-range orientational order within the LC molecules. The origin of this effect lies in electron π–π stacking and is achieved through the matching of the benzene rings of LC molecules to the Gr honeycomb pattern. The interesting effect of this anchoring is a substantial charge transfer from the LC molecule to the honeycomb pattern of the carbon atoms in the Gr anisotropic domain and a reduction in suspension energy. Also, the presence of Fe_3O_4 nanoclusters, through increasing the porosity of the MLG, contributes to this function. This phenomenon can be considered a factor in increasing the conductivity in the LC. Contrarily, this orientational order is locally disturbed by increasing

the concentration of GMN dopant in the LC and aggregates formation. This phenomenon is confirmed by the Cole–Cole diagrams in Fig. 4a.

For more clarity, we address mentioned phenomena by the schematics prepared in Fig. 5. Figure 5a shows the matching of LC benzene rings with the honeycomb pattern of Gr. In Fig. 5b, we can also see the corrugated layer of Gr acts as an alignment layer for LC molecules. In both of Fig. 5a,b, the edges of Gr, due to the electrostatic field, purify the LC from the charged species that were added to the LC due to the passage of time or through different manufacturing processes. But the interesting effect happened in Fig. 5c, which shows metal-oxide nanoclusters that affected the van der Waals attraction between the Gr layers to some extent. This effect has provided the multi-layered structure of Gr with more porosity for anchoring the LC components and enhances its molecules' orientational order. Furthermore, at the points where nanoclusters present and especially at the edges of Gr, there are defects that create more attraction for charged species (different colored spheres have been used to indicate defects and charged species) of the LC and, at sufficiently low frequencies of the applied electric field, form networks for charge transfer to Gr sheets. The set of these phenomena leads to a substantial charge transfer to the Gr surface, especially on its edges and supports its layers as electric dipoles in the dielectric medium. We prepared a color map showing the charge distribution on the Gr sheets in Fig. 5b,c. The hypothetical values of each color have been identified in the lower-left corner of Fig. 5. In Fig. 5b, the boundaries of this color pattern are limited around the LC molecules on the surface of Gr. But in Fig. 5c, the addition of nanoclusters and the processes attributed to them in the presence of the applied electric field has increased the intensity of this color map, especially at the edges of Gr sheet.

Here, in the first category, (0.01–1 w%) samples, based on the results of POM analysis, it has been observed that as the concentration of GMN increases to 0.01%, aggregation occurs between these GMN dopants. As a result, the amount of available surface decreases and the adsorption of ionic impurities onto GMN dopants decreases. This leads to a decrease in electrical conductivity compared to lower concentrations in which smaller aggregation occurred between GMN dopants. In the second category, (0.0001–0.001 w%) samples, it is also possible to highlight the profound effect of separate small dipoles of multi-layered Gr on the reaction to the electric field and even the 0.0001 w% sample may be introduced as the optimal concentration among the others, in terms of the effect on the electrical parameters of the suspension.

Conclusion

In summary, we demonstrated aggregate formation by adding different concentrations of GMN, (0.0001–1 w%) to E7 nematic LC using POM. Also, using the powerful impedance spectroscopy tool, we studied the electrical parameters of GMN-doped samples and have shown that the electrical conductivity of these samples improved in the range of doping concentrations compared to the pure E7 one. This effect is pronounced especially in the 0.0001 w% sample. We attributed it to the reduction in aggregate formation and also the presence of metal-oxide nanoclusters between Gr layers. These factors provide the Gr surface with a large area for interaction and make it active through substantial charge transfer. For future works, considering the magnetic properties of Fe_3O_4 nanoclusters, it is suggested to investigate the electrical properties of the sample with optimum concentration of GMN dopant in the presence of a magnetic field. It is also possible to check the memory effects of such a fluid by sweeping the electric field at a higher amplitude.

Methods

In this study, the nanocomposite of porous expanded multi-layer Gr structure with Fe_3O_4 nanoclusters entrapped between the Gr layers, Gr/metal-oxide-nanocomposite (GMN), was utilized as the dopant to the commonly known, E7 nematic LC with nematic to isotropic temperature 58 °C.

GMN fabrication. The GMN production process is based on a simultaneous electrochemical exfoliation/deposition procedure by using a two-electrode system with nickel as the cathode electrode and graphite foil as the anode electrode. $FeSO_4{\cdot}7H_2O$ powder (5.56 g) and NaOH tablets (2.8 g) dissolved in distilled (DI) water (200 ml), were used to prepare the electrolyte. Controlling the electrode potentials results in the expansion, exfoliation of graphite, and deposition of iron oxide nanoclusters between Gr layers. After 3 h of DC bias (10 V), the achieved product is collected by a magnet from the solution, washed with DI water, and dried at 100 °C.

Suspension preparation. To prepare suspensions with different concentrations of nanocomposite in E7, 2 mg of GMN powder was dispersed in 60 ml of methanol and sonicated in the ultrasonic bath for 1 h. Then we added specific amounts of this dispersion to the E7 at the isotropic temperature. The resulting compounds were further sonicated in the bath at 75 °C for 2 h until the GMN had dispersed in the E7. To evaporate the remaining methanol, we put the resulting suspensions in the oven at 135 °C for 2 h. The final suspensions obtain with four concentrations of 1 w%, 0.01 w%, 0.001 w%, and 0.0001 w% of GMN in E7.

Sample preparation. For impedance characterization, freshly prepared suspensions were filled at 70 °C into PVA-coated test cells with a 38 μm cell gap, 1 cm^2 electrode area, and antiparallel rubbing for planar alignment with the capillary method. For comparison, another cell with the same structural properties is filled with pure E7. For convenience, the samples with different concentrations of GMN will be abbreviated as 1 w% sample, 0.01 w% sample, 0.001 w% sample, and 0.0001 w% sample in the text.

Characterization. The imaging of the nanocomposite was obtained by using field emission scanning electron microscope (FESEM) and tunneling electron microscopy (TEM). The crystallinity of nanocomposite con-

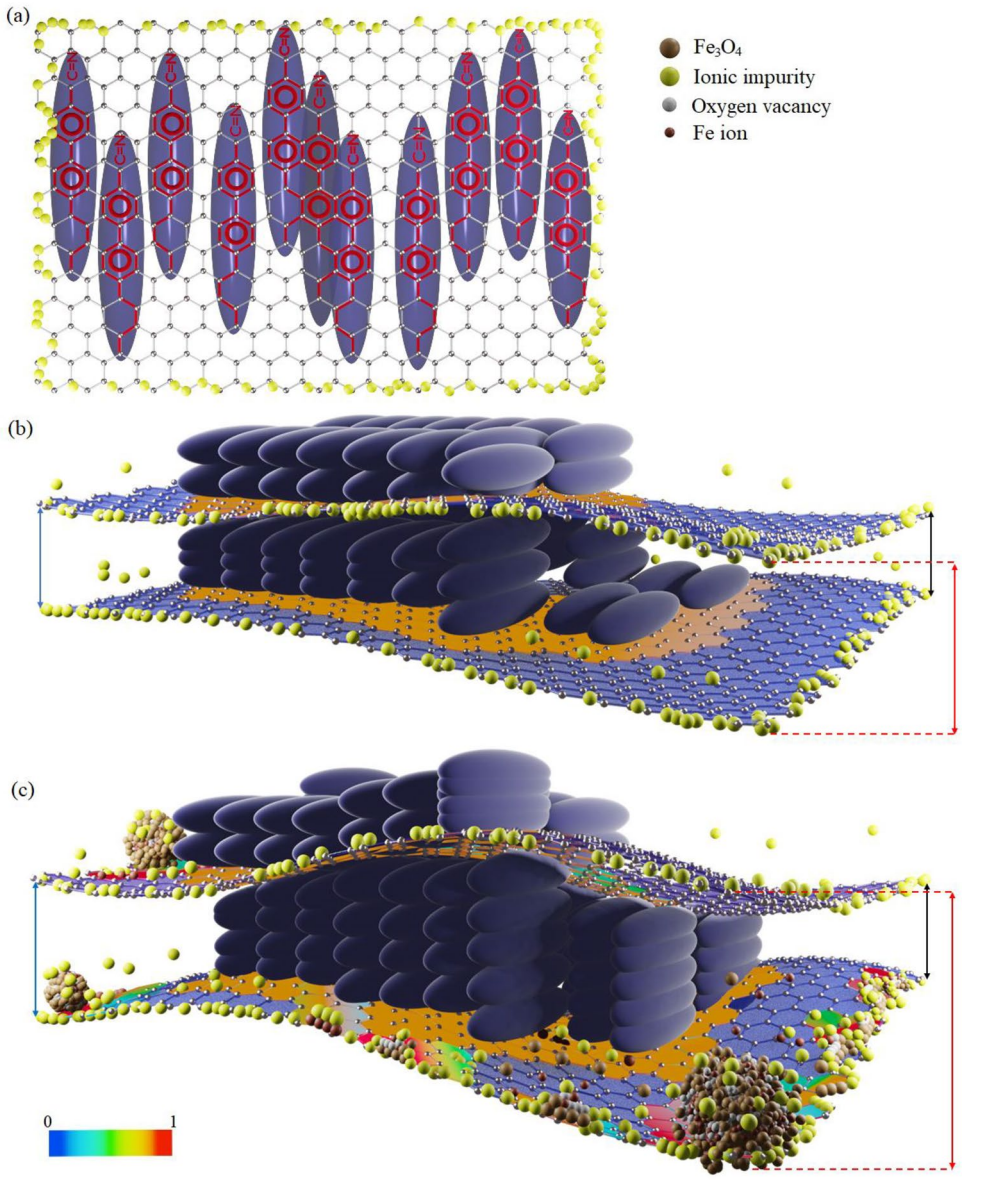

Figure 5. The extended plane composed of repeating unit cells in the shape of a hexagon with carbon atoms at its corners represents the Gr sheet and the blue ellipsoids represent the LC molecules. (**a**) Matching of the benzene rings of LC molecules to the Gr honeycomb pattern and ion trapping effect at the edges of the Gr sheet. (**b**) Corrugated multi-layer structure of Gr exerts another anchoring to the LC components and induces short-range orientational order within LC molecules, and (**c**) the presence of metal-oxide nanoclusters, defects, and oxygen vacancies between Gr successive layers formation prevent their agglomeration. For clarity, the upper-right corner of the figure shows the defect, charged species, and metal-oxides with colored spheres which are larger than the dimensions used in the Gr sheet. The charge transfer has been indicated by a color map on the surface of Gr, with its density specified with different colors of a color box located at the lower-left corner of the figure. The associated numbers of the color box are representatives of the minimum and maximum of this phenomenon, respectively. In part (**b**), charge transfer is due to the presence of LC molecules on the surface of Gr. Furthermore, in part (**c**), the addition of metal-oxide nanoclusters and the defects through them leads to the formation of conductive pathways and charge transfer to the Gr sheets at sufficiently low frequencies of the applied electric field. This phenomenon is pronounced at the edges of Gr and turns it into an electric dipole, indicated by the different colors of the color box around the nanoclusters.

firms using the X-ray diffraction (XRD) patterns. For all of the prepared samples impedance spectroscopy and conductivity measurements were recorded using a sine-like voltage with an amplitude of 0.3 V (RMS) and a frequency in the range of (100 mHz–1 MHz) applied to cells in out of plane manner utilizing NOVA model

2.1.5 (Made in the Netherlands) connected to a personal computer. The texture of the GMN-doped samples was observed using a POM when the cells were between parallel polarizer and analyzer. All measurements were done in the nematic phase at room temperature (RT).

Data availability

The data supporting the findings of this study are available from the corresponding author upon request.

Received: 4 March 2023; Accepted: 4 July 2023
Published online: 19 July 2023

References

1. Mohammadimasoudi, M., Hens, Z. & Neyts, K. Full alignment of dispersed colloidal nanorods by alternating electric fields. *RSC Adv.* **6**, 55736–55744 (2016).
2. Prakash, J., Chandran, A. & Biradar, A. M. Scientific developments of liquid crystal-based optical memory: A review. *Rep. Prog. Phys.* **80**, 16601 (2016).
3. Ji, Y., Fan, F., Xu, S., Yu, J. & Chang, S. Manipulation enhancement of terahertz liquid crystal phase shifter magnetically induced by ferromagnetic nanoparticles. *Nanoscale* **11**, 4933–4941 (2019).
4. Ye, L. *et al.* The influence of Ag nanoparticles on random laser from dye-doped nematic liquid crystals. *Laser Phys. Lett.* **13**, 105001 (2016).
5. Mertelj, A. & Lisjak, D. Ferromagnetic nematic liquid crystals. *Liq. Cryst. Rev.* **5**, 1–33 (2017).
6. Dalir, N., Javadian, S., Kakemam, J. & Sadrpoor, S. M. Enhance the electrical conductivity and charge storage of nematic phase by doping 0D photoluminescent graphene was prepared with small organic molecule as a new array quantum dot liquid crystal displays. *J. Mol. Liq.* **276**, 290–295 (2019).
7. Garbovskiy, Y. Time-dependent electrical properties of liquid crystal cells: Unravelling the origin of ion generation. *Liq. Cryst.* **45**, 1540–1548 (2018).
8. Basu, R. & Atwood, L. J. Two-dimensional hexagonal boron nitride nanosheet as the planar-alignment agent in a liquid crystal-based electro-optic device. *Opt. Express* **27**, 282–292 (2019).
9. Peterson, M. S. E., Georgiev, G., Atherton, T. J. & Cebe, P. Dielectric analysis of the interaction of nematic liquid crystals with carbon nanotubes. *Liq. Cryst.* **45**, 450–458 (2018).
10. SJ, S., Gupta, R. K. & Kumar, S. Effect of functionalised silver nanoparticle on the elastic constants and ionic transport of a nematic liquid crystal. *Liq. Cryst.* **46**, 1868–1876 (2019).
11. Urbanski, M. & Lagerwall, J. P. F. Nanoparticles dispersed in liquid crystals: Impact on conductivity, low-frequency relaxation and electro-optical performance. *J. Mater. Chem. C* **4**, 3485–3491 (2016).
12. Singh, D., Singh, U. B., Dhar, R., Dabrowski, R. & Pandey, M. B. Enhancement of electro-optical and dielectric parameters of a room temperature nematic liquid crystalline material by dispersing multi-walled carbon nanotubes. *Liq. Cryst.* **48**, 307–312 (2021).
13. Dalir, N., Javadian, S., Kakemam, J. & Yousefi, A. Evolution of electro-chemical and electro-optical properties of nematic liquid crystal doped with graphene oxide. *J. Mol. Liq.* **265**, 398–407 (2018).
14. Garbovskiy, Y. & Glushchenko, I. Nano-objects and ions in liquid crystals: Ion trapping effect and related phenomena. *Crystals* **5**, 501–533 (2015).
15. Mohammad, A. & Inamuddin, D. *Green Solvents II: Properties and Applications of Ionic Liquids* Vol. 2 (Springer, 2012).
16. Hsu, C.-J., Lin, L.-J., Huang, M.-K. & Huang, C.-Y. Electro-optical effect of gold nanoparticle dispersed in nematic liquid crystals. *Crystals* **7**, 287 (2017).
17. Dalir, N. & Javadian, S. Evolution of morphology and electrochemical properties of colloidal nematic liquid crystal doped with carbon nanotubes and magnetite. *J. Mol. Liq.* **287**, 110927 (2019).
18. Studenyak, I. P., Kopčanský, P., Timko, M., Mitroova, Z. & Kovalchuk, O. V. Effects of non-additive conductivity variation for a nematic liquid crystal caused by magnetite and carbon nanotubes at various scales. *Liq. Cryst.* **44**, 1709–1716 (2017).
19. Tomylko, S., Yaroshchuk, O., Koval'Chuk, O. & Lebovka, N. Structural evolution and dielectric properties of suspensions of carbon nanotubes in nematic liquid crystals. *Phys. Chem. Chem. Phys.* **19**, 16456–16463 (2017).
20. Garbovskiy, Y. Conventional and unconventional ionic phenomena in tunable soft materials made of liquid crystals and nanoparticles. *Nano Express* **2**, 12004 (2021).
21. Garbovskiy, Y. Impact of contaminated nanoparticles on the non-monotonous change in the concentration of mobile ions in liquid crystals. *Liq. Cryst.* **43**, 664–670 (2016).
22. Basu, R. Effects of graphene on electro-optic switching and spontaneous polarization of a ferroelectric liquid crystal. *Appl. Phys. Lett.* **105**, 112905 (2014).
23. Ayeb, H. *et al.* Dielectrical, electro-optical and textural studies of 5CB nematic liquid crystal doped with TiO_2 and Cu-TiO_2 nanoparticle. *Liq. Cryst.* **48**, 223–232 (2021).
24. SJ, S., Gupta, R. K., Kumar, S. & Manjuladevi, V. Enhanced electro-optical response of nematic liquid crystal doped with functionalised silver nanoparticles in twisted nematic configuration. *Liq. Cryst.* **47**, 1678–1690 (2020).
25. Singh, P. K., Dubey, P., Dhar, R. & Dabrowski, R. Functionalized and non-functionalized multi walled carbon nanotubes in the anisotropic media of liquid crystalline material. *J. Mol. Liq.* **369**, 120889 (2023).
26. Cheng, Y., Fan, Y., Pei, Y. & Qiao, M. Graphene-supported metal/metal oxide nanohybrids: synthesis and applications in heterogeneous catalysis. *Catal. Sci. Technol.* **5**, 3903–3916 (2015).
27. Lapanik, V., Timofeev, S. & Haase, W. Electro-optic properties of nematic and ferroelectric liquid crystalline nanocolloids doped with partially reduced graphene oxide. *Phase Transitions* **89**, 133–143 (2016).
28. Wu, P.-C. & Lee, W. Phase and dielectric behaviors of a polymorphic liquid crystal doped with graphene nanoplatelets. *Appl. Phys. Lett.* **102**, 162904 (2013).
29. Jung, Y. U., Park, K.-W., Hur, S.-T., Choi, S.-W. & Kang, S. J. High-transmittance liquid-crystal displays using graphene conducting layers. *Liq. Cryst.* **41**, 101–105 (2014).
30. Basu, R., Garvey, A. & Kinnamon, D. Effects of graphene on electro-optic response and ion-transport in a nematic liquid crystal. *J. Appl. Phys.* **117**, 74301 (2015).
31. Wu, P.-C., Lisetski, L. N. & Lee, W. Suppressed ionic effect and low-frequency texture transitions in a cholesteric liquid crystal doped with graphene nanoplatelets. *Opt. Express* **23**, 11195–11204 (2015).
32. Basu, R. & Lee, A. Ion trapping by the graphene electrode in a graphene-ITO hybrid liquid crystal cell. *Appl. Phys. Lett.* **111**, 161905 (2017).
33. Basu, R. Graphene as an alignment agent, an electrode, and a source of surface chirality in a smectic-A liquid crystal. *Phys. Rev. E* **103**, 22710 (2021).
34. Blake, P. *et al.* Graphene-based liquid crystal device. *Nano Lett.* **8**, 1704–1708 (2008).

35. Wang, L. *et al.* Broadband tunable liquid crystal terahertz waveplates driven with porous graphene electrodes. *Light Sci. Appl.* **4**, e253 (2015).
36. Qasim, M. M. *et al.* Hybrid graphene nematic liquid crystal light scattering device. *Nanoscale* **7**, 14114–14120 (2015).
37. Basu, R., Kinnamon, D. & Garvey, A. Graphene and liquid crystal mediated interactions. *Liq. Cryst.* **43**, 2375–2390 (2016).
38. Basu, R., Kinnamon, D. & Garvey, A. Nano-electromechanical rotation of graphene and giant enhancement in dielectric anisotropy in a liquid crystal. *Appl. Phys. Lett.* **106**, 201909 (2015).
39. Yu, D. & Dai, L. Self-assembled graphene/carbon nanotube hybrid films for supercapacitors. *J. Phys. Chem. Lett.* **1**, 467–470 (2010).
40. Wang, Y. *et al.* Supercapacitor devices based on graphene materials. *J. Phys. Chem. C* **113**, 13103–13107 (2009).
41. Jiang, L., Gu, S., Ding, Y., Jiang, F. & Zhang, Z. Facile and novel electrochemical preparation of a graphene–transition metal oxide nanocomposite for ultrasensitive electrochemical sensing of acetaminophen and phenacetin. *Nanoscale* **6**, 207–214 (2014).
42. George, J. M., Antony, A. & Mathew, B. Metal oxide nanoparticles in electrochemical sensing and biosensing: A review. *Microchim. Acta* **185**, 1–26 (2018).
43. Khan, M. *et al.* Graphene based metal and metal oxide nanocomposites: synthesis, properties and their applications. *J. Mater. Chem. A* **3**, 18753–18808 (2015).
44. Zhu, N. *et al.* Graphene as a conductive additive to enhance the high-rate capabilities of electrospun Li4Ti5O12 for lithium-ion batteries. *Electrochim. Acta* **55**, 5813–5818 (2010).
45. Li, M., Cheng, J. P., Wang, J., Liu, F. & Zhang, X. B. The growth of nickel-manganese and cobalt-manganese layered double hydroxides on reduced graphene oxide for supercapacitor. *Electrochim. Acta* **206**, 108–115 (2016).
46. Morales, D. M. *et al.* Trimetallic Mn-Fe-Ni oxide nanoparticles supported on multi-walled carbon nanotubes as high-performance bifunctional ORR/OER electrocatalyst in alkaline media. *Adv. Funct. Mater.* **30**, 1905992 (2020).
47. Sheykhifar, Z. & Mohseni, S. M. Highly light-tunable memristors in solution-processed 2D materials/metal composites. *Sci. Rep.* **12**, 18771 (2022).
48. Mohammad, B. *et al.* State of the art of metal oxide memristor devices. *Nanotechnol. Rev.* **5**, 311–329 (2016).
49. Di Martino, G. *et al.* Real-time in situ optical tracking of oxygen vacancy migration in memristors. *Nat. Electron.* **3**, 687–693 (2020).
50. Parvez, K. *et al.* Exfoliation of graphite into graphene in aqueous solutions of inorganic salts. *J. Am. Chem. Soc.* **136**, 6083–6091 (2014).
51. Ansari, N., Payami, Z. & Feghhi, F. Synthesis of iron/graphene composites with controlled magnetization by electrochemical exfoliation/deposition using sodium dodecyl sulfate as surfactant. *J. Magn. Magn. Mater.* **500**, 166398 (2020).
52. Hajiali, M. *et al.* Controlling magnetization of Gr/Ni composite for application in high-performance magnetic sensors. *ACS Appl. Electron. Mater.* **1**, 2502–2513 (2019).
53. Ansari, N. *et al.* Facile synthesis of water-stable iron intercalated multi layered graphene nanocomposite with large magnetic moments as superior water pollutant remediators. *Synth. Met.* **255**, 116105 (2019).
54. Chuang, C.-H. *et al.* A green, simple and cost-effective approach to synthesize high quality graphene by electrochemical exfoliation via process optimization. *RSC Adv.* **5**, 54762–54768 (2015).
55. Yadav, S. P. & Singh, S. Carbon nanotube dispersion in nematic liquid crystals: An overview. *Prog. Mater. Sci.* **80**, 38–76 (2016).
56. Zafra, J. C. T., Garcilópez, I. A. P., Del Pozo, V. U., Pena, J. M. S. & Lucas, C. M. Electrical modeling of tristate antiferroelectric liquid crystal devices. *Opt. Eng.* **50**, 81206 (2011).
57. Belyaev, B. A., Drokin, N. A. & Maslennikov, A. N. Impedance spectroscopy investigation of liquid crystals doped with ionic surfactants. *Phys. Solid State* **56**, 1455–1462 (2014).
58. Sprokel, G. J. Resistivity, permittivity and the electrode space charge of nematic liquid crystals. *Mol. Cryst. Liq. Cryst.* **22**, 249–260 (1973).
59. Belyaev, B. A. & Drokin, N. A. Impedance spectroscopy investigation of electrophysical characteristics of the electrode-liquid crystal interface. *Phys. Solid State* **57**, 181–187 (2015).
60. Karaawi, A. R. *et al.* Direct current electric conductivity of ferroelectric liquid crystals–gold nanoparticles dispersion measured with capacitive current technique. *Liq. Cryst.* **47**, 1507–1515 (2020).
61. Kocman, M., Pykal, M. & Jurečka, P. Electric quadrupole moment of graphene and its effect on intermolecular interactions. *Phys. Chem. Chem. Phys.* **16**, 3144–3152 (2014).
62. Ghasemi, R. *et al.* Metal/metal-oxide thin layer heterostructure by laser treatment for memristor application. *Mater. Lett.* **261**, 127094 (2020).
63. Wan, X. *et al.* Bio-mimicked atomic-layer-deposited iron oxide-based memristor with synaptic potentiation and depression functions. *Jpn. J. Appl. Phys.* **57**, 60303 (2018).

Author contributions

M.K., F.F. and A.G. did the main experiment job, M.K., N.D., N.A., M.M. and S.M.M. analyzed the results, M.K., S.M.M. and M.K. wrote the main manuscript text and A.F.N. prepared the graphics. All authors reviewed the manuscript.

Competing interests

The authors declare no competing interests.

Additional information

Supplementary Information The online version contains supplementary material available at https://doi.org/10.1038/s41598-023-38157-y.

Correspondence and requests for materials should be addressed to M.K. or S.M.

Reprints and permissions information is available at www.nature.com/reprints.

Publisher's note Springer Nature remains neutral with regard to jurisdictional claims in published maps and institutional affiliations.